*Article*

# Hybrid Gold-Based Perovskite Derivatives: Synthesis, Properties, and Prospects in Photovoltaics

Chang Liu [1,2,3,4], Xifeng Fu [1,4,5], Zi-Ang Nan [5], Zilong Zhang [2,3], Lingyi Meng [1,2,4,5] and Peng Gao [1,2,3,4,*]

[1] College of Chemistry and Materials Science, Fujian Normal University, Fuzhou 350007, China
[2] CAS Key Laboratory of Design and Assembly of Functional Nanostructures, Fujian Institute of Research on the Structure of Matter, Chinese Academy of Sciences, Fuzhou 350002, China
[3] Laboratory for Advanced Functional Materials, Xiamen Institute of Rare Earth Materials, Haixi Institute, Chinese Academy of Sciences, Xiamen 361021, China
[4] Fujian College, University of Chinese Academy of Sciences, Fuzhou 350002, China
[5] Fujian Institute of Research on the Structure of Matter, Chinese Academy of Sciences, Fuzhou 350002, China
* Correspondence: peng.gao@fjirsm.ac.cn

**Abstract:** Hybrid gold-based perovskite derivatives typically exhibit low optical bandgaps and high optical absorption coefficients, rendering them promising for photovoltaic applications. In this study, we successfully synthesized six new hybrid gold-based perovskite derivatives, namely $[(C_6H_8N_2)(AuI_4)(AuI_2)]$(**3AMPY**), $[(C_6H_{14}N_2)(AuI_4)(AuI_2)]$(**3AMP**), $[(C_8H_{12}N)(AuI_4)]$(**2PEAI**), $[(C_4H_{14}N_2O)(AuI_4)_2]$(**OBA**), $[(C_6H_{18}N_2O_2)_3(AuI_4)_4(I_3)_2]$(**DDA**), and $[(C_{10}H_{26}N_2O_3)(AuI_4)(I_3)]$(**TOTA**), through a straightforward and efficient hydrothermal method, achieving millimeter-sized single crystals. The structural analysis of the single crystals revealed variations in crystal structures arising from differences in constituent units and their spatial positioning relationships. First-principles calculations ascertained their high optical absorption coefficients in the visible light spectrum and indirect bandgap properties. Theoretical models indicated that the spectroscopic limited maximum efficiency (SLME) values of **3AMPY**, **2PEAI**, **DDA**, and **TOTA** approached approximately 30% in films of 0.5 μm thickness, signifying their potential candidacy as solar cell absorbers.

**Keywords:** gold-based perovskite; perovskite-derivative properties; single crystal; first-principles calculations; solar cells

## 1. Introduction

Over the past twenty years, scientists have conducted intensive research to find economically friendly clean energy materials. In this context, perovskite materials have become a research hotspot for the next generation of energy-conversion semiconductor materials due to their superior economic properties, small exciton binding energy, long carrier diffusion length and lifetime, ease of solution processing, and tunable bandgap [1]. Based on these advantages, perovskite materials can be applied to various optoelectronic devices, such as solar cells [2–4], photodetectors [5], light-emitting diodes (LEDs) [6], etc. However, the toxicity and instability of traditional lead-based perovskite materials have become the main factors limiting their further development [7–9]. Therefore, researchers have been committed to finding new B-site elements to replace lead and develop environmentally friendly halide perovskite and perovskite-derivative materials [10].

Gold-based perovskite, as an environmentally friendly material, boasts good stability and a high optical absorption coefficient, among other advantages [11]. Additionally, gold elements in the perovskite structure can exist in multiple oxidation states, maintaining the stability of the B-site gold element. Various gold-based perovskite derivatives can be synthesized by substituting A-site cations and X-site halide anions. Therefore, gold-based perovskites exhibit rich diversity, giving researchers a broad scope. Gold-based perovskites were first reported in the early 20th century, when Gupta and colleagues first discovered

$Cs_2Au^IAu^{III}I_6$ [12]. Subsequently, after more than a century of development, various new types of pure gold-based perovskites have been synthesized and extensively studied, such as $K_2Au^IAu^{III}I_6$, $Rb_2Au^IAu^{III}Br_6$ [13], $LiAuI_4$, and $RbAuCl_4$ [14]. Recently, Kojima et al. found that the perovskite Cs2AuIAuIIII6 transitions from semiconductor to metallic properties under high-temperature and high-pressure conditions [15]. Theoretical calculations by Debbichi et al. suggested that $Cs_2Au^IAu^{III}I_6$ possesses an appropriate bandgap and high optical absorption coefficient, potentially achieving over 20% photo-conversion efficiency (PCE) [16]. Additionally, Li et al. predicted a series of novel gold-based perovskites as promising solar cell absorbers, $Cs_2Au^ISbCl_6$, $Cs_2Au^IInCl_6$, and $Cs_2Au^IBiCl_6$ exhibiting a spectroscopic limited maximum efficiency (SLME) of approximately 30% in a 0.5 mm thick film [17].

Recently, there has been a growing number of reports on organic–inorganic hybrid gold-based perovskites and their derivatives. In 2021, Fan et al. synthesized a series of narrow-bandgap hybrid organic–inorganic gold-based perovskites and their derivatives via a simple and efficient hydrothermal method, revealing their potential applications in the optoelectronic field [18]. In 2024, Walusiak et al. reported a series of organic–inorganic hybrid gold-based perovskite derivatives and investigated their crystal structures and chemical properties [19]. According to previous studies, these gold-based perovskite derivatives tend to form low-dimensional structures, typically containing $[Au^II_2]$ and $[Au^{III}I_4]$ units composed of gold cations and iodide anions in their structures [20]. These structural units exhibit strong intermolecular interactions, typically resulting in hybrid gold-based perovskite derivatives being dark-colored narrow-bandgap semiconductors. This makes them potential candidates for light-absorbing layer materials in solar cells, with related device studies demonstrating their potential application as solar cell absorbers [11,21].

However, despite the potential application values of organic–inorganic hybrid perovskites and their derivatives, reports on such materials are still limited, and research on them is relatively scattered. Therefore, it is essential to expand the variety of hybrid organic–inorganic perovskites and their derivatives further and explore their application potential. In this paper, we report six new organic–inorganic gold-based hybrid perovskite derivatives and have named these compounds based on the English abbreviations of their A-site cations: $[(C_6H_8N_2)(AuI_4)(AuI_2)]$(**3AMPY**), $[(C_6H_{14}N_2)(AuI_4)(AuI_2)]$(**3AMP**), $[(C_8H_{12}N)(AuI_4)]$(**2PEAI**), $[(C_4H_{14}N_2O)(AuI_4)_2]$(**OBA**), $[(C_6H_{18}N_2O_2)_3(AuI_4)_4(I_3)_2]$(**DDA**), and $[(C_{10}H_{26}N_2O_3)(AuI_4)(I_3)]$(**TOTA**). Among these six compounds, **3AMP** contains $[Au^{III}I_6]$ octahedra, forming a zero-dimensional perovskite-like structure. In contrast, the remaining five compounds exhibit zero-dimensional non-perovskite structures. We obtained millimeter-sized single crystals of these gold-based perovskite derivatives by optimizing the hydrothermal reaction parameters. Then, we combined experimental characterization with theoretical calculations to study these materials' crystal structures, electrical properties, thermal stability, and optical properties. The results indicated that these compounds are narrow-bandgap materials with good thermal stability. First-principles calculations showed that these materials exhibited strong, light absorption coefficients in the visible light region, with SLME values reaching around 30% for **3AMPY**, **2PEAI**, **DDA**, and **TOTA**, suggesting significant potential for applications in the field of solar cells. We believe our work can further advance the research and application of organic–inorganic hybrid gold-based perovskite derivatives.

## 2. Results and Discussions

### 2.1. The Synthesis Process of Single Crystals

Using a straightforward and efficient hydrothermal reaction, we successfully prepared millimeter-scale single crystals of six organic–inorganic gold-based hybrid perovskite derivatives. The single-crystal (SC) synthesis process is shown in Figure 1a, taking the preparation of $[(C_4H_{14}N_2O)(AuI_4)_2]$ (**OBA**) as an example. An amount of 1 mmol of $HAuCl_4\cdot4H_2O$ (0.412 g) was dissolved in an appropriate amount of deionized water, stirred for 5 min to completely dissolve $HAuCl_4\cdot4H_2O$, and then 1 mmol (0.64 µL) of 2,2′-

oxydiethylamine (OBA) was added, causing a noticeable reaction (generation of micro-SCs. Then, add 0.5 mL of hydroiodic acid (hydroiodic acid must be in excess to ensure the complete reaction of the reactants). After thoroughly stirring the reaction solution, transfer it to a reaction vessel lined with polytetrafluoroethylene and conduct a hydrothermal reaction in a temperature-controlled oven at 90 °C for 24 h. Then, slowly cool the reaction mixture to room temperature at 2 °C/h to obtain the SCs. As shown in Figure 1b, all SCs were black and had polyhedral shapes, with crystal sizes in the millimeter range.
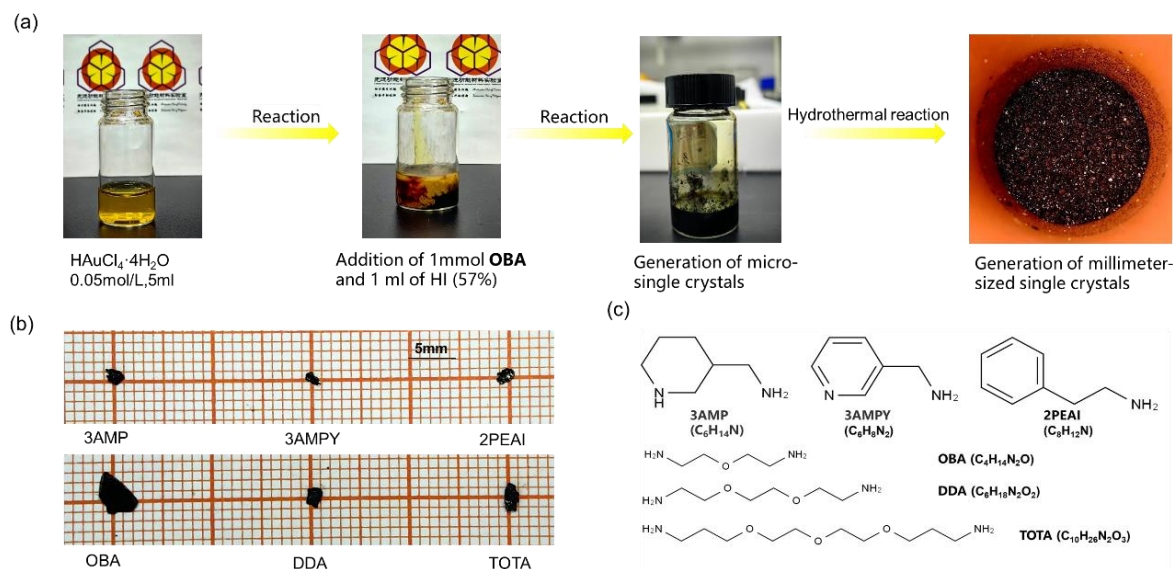


**Figure 1.** (**a**) Single-crystal synthesis process of $[(C_4H_{14}N_2O)\,(AuI_4)_2]$ (**OBA**). (**b**) Millimeter-scale single-crystal images of hybrid gold-based perovskite derivatives. (**c**) The A-site cation organics used in the reaction.

Subsequently, the single crystals were washed with deionized water and placed in an 80 °C oven to dry to remove any surface-adhered elemental $I_2$. Single crystals of six compounds were obtained by replacing the organic component in the reaction system. The organic components used in this work are shown in Figure 1c. The control-of-variables experiment determined the above reaction parameters. According to the experience results, a low hydrothermal reaction temperature (below 60 °C) will result in insufficient energy in the reaction system, leading to the inability to generate single crystals.

Conversely, a high temperature (above 150 °C) can cause the decomposition of reaction products and the generation of elemental Au byproducts, as shown in Figure S1. Therefore, around 100 °C is an appropriate temperature for synthesizing single crystals in this series. The synthesis of other crystals was also based on this temperature. Furthermore, we found that properly reducing the cooling rate was beneficial for increasing the yield of single crystals. To balance the yield of single crystals with the reaction duration, we finally set the reaction conditions: reaction temperature of 90 °C, incubation for 24 h, and slow cooling to room temperature at 2 °C/h. In our attempts to prepare thin films by redissolving those hybrid gold-based perovskite derivatives and via spin coating, we encountered solubility issues in most polar solvents and poor film formations, which is one of the challenges faced by many gold–iodide compounds. We are currently exploring the relevant film preparation technology to prepare solar cell devices in the lab.

## 2.2. The Analysis of Single-Crystal Structures

We conducted an X-ray single-crystal diffraction analysis on the six compounds, and their crystal structures are illustrated in Figure 2. Among them, **3AMP**, **2PEAI**, **OBA**, and **TOTA** belong to the monoclinic crystal system, exhibiting relatively good symmetry, while **3AMPY** and **DDA** belong to the triclinic crystal system, displaying lower symmetry.

The specific crystal structure parameters of six kinds of gold-based perovskite derivates are summarized in Table 1. The more specific crystallographic data are presented in Tables S1 and S2.
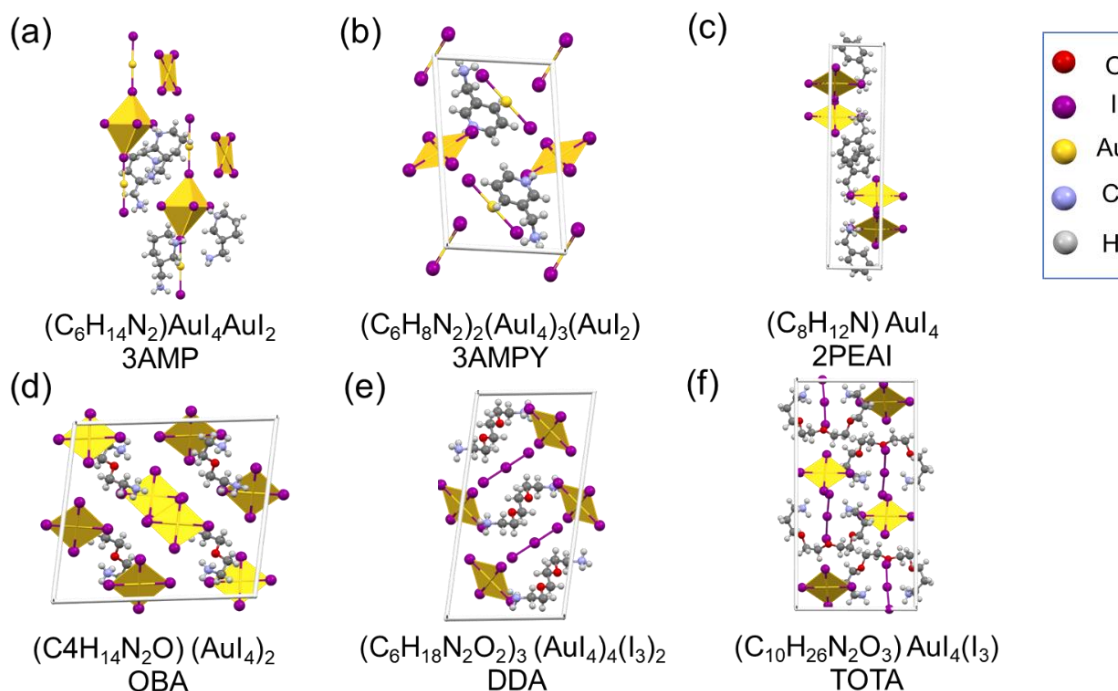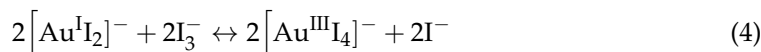


**Figure 2.** (**a**–**f**) The schematic diagrams of the single-crystal structures of the hybrid gold-based perovskite derivates.

**Table 1.** Crystallographic parameters for hybrid gold-based perovskite derivates.

| | 2PEAI | 3AMP | 3AMPY | OBA | DDA | TOTA |
|---|---|---|---|---|---|---|
| Formula | $C_8H_{12}N$ $(AuI_4)$ | $C_6H_{14}N_2(AuI_4)$ $(AuI_2)$ | $C_6H_8N_2$ $(AuI_4)(AuI_2)$ | $C_4H_{14}N_2O$ $(AuI_4)_2$ | $(C_6H_{18}N_2O_2)_3$ $(AuI_4)_4(I_3)_2$ | $C_{10}H_{26}N_2O_3$ $(AuI_4)(I_3)$ |
| Crystal system | monoclinic | monoclinic | triclinic | monoclinic | triclinic | monoclinic |
| Space group | $P2_1/c$ (14) | $Cm$ (8) | $P\bar{1}$ (2) | $P2_1/c$ (14) | $P\bar{1}$ (2) | $P2_1/n$ (14) |
| a, Å | 6.025 (4) | 19.084 (2) | 8.3376 (3) | 15.7263 (8) | 8.1710 (5) | 9.1421 (5) |
| b, Å | 25.425 (13) | 8.3142 (9) | 9.3799 (3) | 8.8418 (4) | 10.8475 (8) | 24.0782 (12) |
| c, Å | 9.2683 (6) | 13.762 (2) | 14.0131 (5) | 17.2007 (8) | 20.3167 (14) | 12.9102 (6) |
| α, ° | 90 | 90 | 90.1030(10) | 90 | 80.611(3) | 90 |
| β, ° | 92.634 (2) | 111.702 (5) | 103.457 (2) | 98.458 (2) | 85.264 (3) | 102.001 (2) |
| γ−γ | 90 | 90 | 115.317(10) | 90 | 73.480(3) | 90 |
| Volume, Å3 | 1418.5 (15) | 2028.8 (4) | 957.03 (6) | 2365.7 (2) | 1702.1 (2) | 2779.7 (2) |
| Z | 4 | 2 | 2 | 4 | 2 | 4 |
| Radiation, Å | MoKα ($\lambda = 0.71073$ Å) | MoKα ($\lambda = 0.71073$ Å) | MoKα ($\lambda = 0.71073$ Å) | MoKα ($\lambda = 0.71073$ Å) | MoKα ($\lambda = 0.71073$ Å) | MoKα ($\lambda = 0.71073$ Å) |
| Temp., K | 200.00 | 200.00 | 200.00 | 200.00 | 200.00 | 200.00 |

Analyzing the composition of each crystal structure, we found three types of structural units, apart from the organic cations, including the $[Au^II_2]^-$, $[Au^{III}I_4]^-$, and $[I_3]^-$ units, composed of $Au^+$ and $Au^{3+}$, and $I^-$, as well as $I^-$ and $I_2$, respectively. We investigated the formation mechanisms of different structural units in gold-based perovskite derivatives

based on the possible redox reactions between Au cations and I anions. Equations (1)–(4), depict the chemical reaction processes as follows:

$$Au^{3+} + 2I^- \leftrightarrow Au^+ + I_2 \tag{1}$$

$$Au^+ + 2I^- \leftrightarrow \left[Au^I I_2\right]^- \tag{2}$$

$$I^- + I_2 \leftrightarrow I_3^- \tag{3}$$

$$2\left[Au^I I_2\right]^- + 2I_3^- \leftrightarrow 2\left[Au^{III} I_4\right]^- + 2I^- \tag{4}$$

As depicted in Equations (1) and (2), in the reaction system, initially, $Au^{3+}$ undergoes oxidation by $I^-$ to form $Au^+$, followed by the reaction of one unit of $Au^+$ with two units of $I^-$ to generate the $[Au^I I_2]^-$ unit [16]. Subsequently, $I^-$ reacts with oxygen in the aqueous solution to form $I_2$, and in the presence of excess $I^-$, the surplus $I^-$ combines with $I_2$ to form the $[I_3^-]$ unit, as shown in Equation (3) [22]. Finally, as indicated in Equation (4), at this stage, the $[Au^I I_2]^-$ unit in the reaction system reacts with the $[I_3]^-$ unit, yielding the $[Au^{III} I_4]^-$ unit [19].

Then, we further investigated the crystal structures of these compounds. The six compounds were classified and analyzed based on the different structural units composing their crystal structures: (1) **3AMP** and **3AMPY**; (2) **DDA** and **TOTA**; and (3) **2PEAI** and **OBA**. The detailed analysis is as follows:

(1)  In the crystal structures of **3AMP** and **3AMPY,** the anions consist of $[Au^I I_2]^-$ and $[Au^{III} I_4]^-$ units. Specifically, **3AMP** comprises $[Au^I I_2]^-$ and $[Au^{III} I_4]^-$ anion units, along with one divalent organic cation to achieve charge balance. It is noteworthy that in **3AMP**, there exists an $[AuI_6]$ octahedron, forming a zero-dimensional perovskite-like structure. These octahedra are connected by $Au\cdots I^-$-Au bonds formed by sharing $I^-$ ions in the vertical direction, with one $[Au^{III} I_4]^-$ unit and two $[Au^I I_2]^-$ units. Otherwise, **3AMPY** comprises three $[Au^I I_2]^-$ and one $[Au^{III} I_4]^-$ anion units, balanced by two divalent organic cations. The $[Au^I I_2]^-$ and $[Au^{III} I_4]^-$ anion units exist independently, forming a zero-dimensional non-perovskite structure. This significant structural difference arises from the distinct spatial distribution of $[Au^I I_2]^-$ and $[Au^{III} I_4]^-$ ions between the two crystals. As shown in Figure 3a, in the crystal structure of **3AMP**, the $[Au^I I_2]^-$ is positioned directly above the center of the $[Au^{III} I_4]^-$ unit. The $Au\cdots I$ bond lengths between adjacent $[Au^I I_2]^-$ and $[Au^{III} I_4]^-$ are 3.336 Å and 3.364 Å, respectively. Therefore, considering the shorter distance between the structural units and appropriate spatial distribution, $[Au^I I_2]^-$ and $[Au^{III} I_4]^-$ can form $[AuI_6]$ octahedra. In the crystal structure of **3AMPY**, the $Au\cdots I$ bond lengths between $[Au^{III} I_4]^-$ and the $[Au^I I_2]^-$ unit positioned directly above it are 3.922 Å and 3.693 Å, respectively. The longer distances render the $Au\cdots I$ bonds unstable, preventing the formation of $[AuI_6]$ octahedra. As a result, $[Au^I I_2]^-$ and $[Au^{III} I_4]^-$ units exist independently without forming an octahedral structure.

(2)  In the **DDA** and **TOTA** crystal structures, the anions consist of $[Au^{III} I_4]^-$ and $[I_3]^-$ units. Specifically, **DDA** is balanced by two $[Au^{III} I_4]^-$ and one $[I_3]^-$ anion units along with two divalent organic cations, while **TOTA** is balanced by one $[Au^{III} I_4]^-$ and one $[I_3]^-$ anion units along with one divalent organic cation. As shown in Figure 4a,b, the length of the $[I_3]^-$ structural unit is 5.876 Å. In both structures, the distance between the adjacent $[Au^{III} I_4]^-$ units is much greater than the length of $[I_3]^-$, allowing for the incorporation of $[I_3]^-$ units. Consistent with previous studies, the presence of $[I_3]^-$ units in hybrid gold-based perovskite derivatives facilitates charge transport. [23] Moreover, the closer the distance between $[I_3]^-$ and $[Au^{III} I_4]^-$ units, the faster the carrier migration along $[I_3]^-$, resulting in better conductivity. This suggests that **DDA** and **TOTA** are expected to exhibit superior conductivity due to their favorable arrangement for charge transport.

(3) In the crystal structures of **2PEAI** and **OBA**, the anions consist of $[Au^{III}I_4]^-$ units. Specifically, **2PEAI** is balanced by one $[Au^{III}I_4]^-$ anion unit and one monovalent organic cation, while **OBA** is balanced by two $[Au^{III}I_4]^-$ anion units and one divalent organic cation. Due to the absence of $[Au^{I}I_2]^-$ units, the $[Au^{III}I_4]^-$ units in these two crystals cannot form octahedra, resulting in zero-dimensional non-perovskite structures. Additionally, as shown in Figure 4c,d, because of the excessively short distances between the adjacent $[Au^{III}I_4]^-$ units, measured at 5.304 Å and 3.496 Å, respectively, $[I_3]^-$ units cannot be accommodated in the structure. As a result, the anions consist solely of $[Au^{III}I_4]^-$ units.
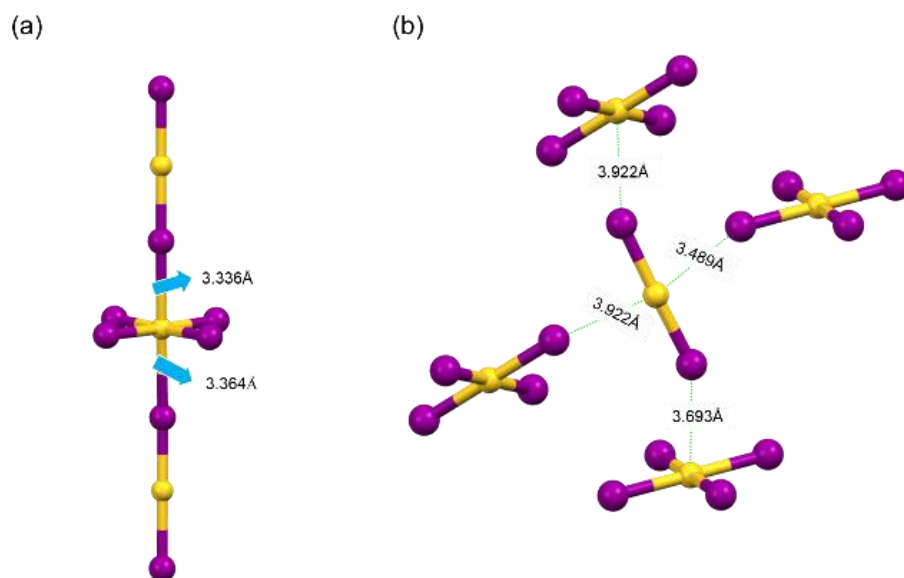


**Figure 3.** The distances of Au···I between the $[Au^{I}I_2]^-$ and $[Au^{III}I_4]^-$ units in **3AMP** (**a**) and **3AMPY** (**b**).
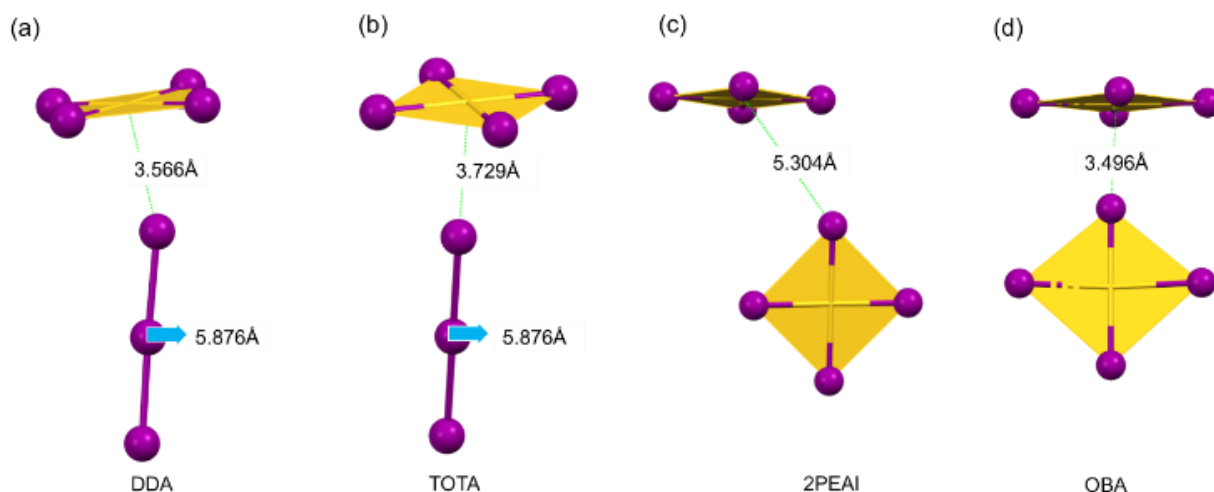


**Figure 4.** The distances of Au···I between adjacent structural units in DDA (**a**), TOTA (**b**), 2PEAI (**c**) and OBA (**d**).

In summary, the differences in crystal structures of these compounds arise from variations in the types of constituent units and their spatial positioning relationship.

Raman spectroscopy is one of the most effective methods for studying the gold valence transitions of various organic–inorganic perovskite derivatives. To further demonstrate the accuracy of the valence state of Au elements in our crystal structure, we obtained the Raman spectra of these compounds through testing, as shown in Figure 5. Analyzing the Raman spectra, we found peaks corresponding to Au-I bonds near 130 cm$^{-1}$ for all

compounds, consistent with the literature reports [23]. Further analysis, as shown in Figure 2a,b, revealed that 3AMP and 3AMPY contain $[Au^{III}I_4]^-$ and $[Au^I I_2]^-$ units, where the Au-I bond length in the $[Au^{III}I_4]^-$ units is longer than that in the $[Au^I I_2]^-$ units (see Figure S2). By comparing the longer Au-I bond in the $[Au^{III}I_4]^-$ units (around 2.62 Å) with that in the $[Au^I I_2]^-$ units (around 2.55 Å), we attributed the lower-lying modes, $A_1$ (127.9 cm$^{-1}$) and $A_2$ (131.2 cm$^{-1}$), to the $[Au^{III}I_4]^-$ units. Furthermore, the higher modes, $B_1$ (130.4 cm$^{-1}$) and $B_2$ (133.8 cm$^{-1}$) are indicative of $[Au^I I_2]^-$ units [24]. Additionally, in 2PEAI, OBA, DDA, and TOTA, the Au ions and I ions form single $[Au^{III}I_4]^-$ units (Figure 2c–f), corresponding to individual Au-I modes ($A_3$, $A_4$, $A_5$, and $A_6$). The results of Raman spectroscopy testing corresponded well with our crystal structure, demonstrating the accuracy of the valence state of Au elements in the crystal structure.
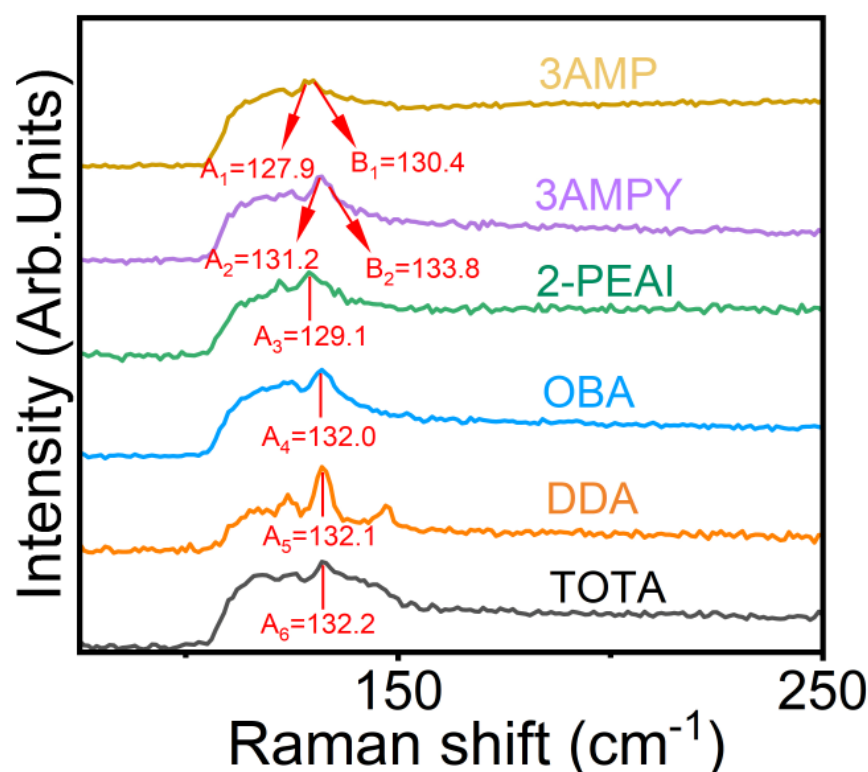


**Figure 5.** Raman spectra for hybrid gold-based perovskite derivatives at 300 K.

*2.3. The Characterization of Optical Properties and Thermal Stability*

To ascertain the purity of the synthesized samples of the six compounds, we ground the single crystals into powder for X-ray diffraction experiments. The powder XRD peaks obtained from the experiment were compared with the theoretical simulated peaks of the single-crystal structures, as shown in Figure 6. The correspondence between the simulated diffraction peaks of the crystal structures and the experimentally obtained diffraction peaks confirmed the high purity of the synthesized materials. This assured the reliability of the subsequent optical, electrical, and thermal stability tests.

Thermal stability is crucial for viable applications in optoelectronics, and a TGA/DTG (Thermogravimetric Analysis/Derivative Thermogravimetry) analysis was conducted on hybrid gold-based perovskite-derivative powders to understand their thermal decomposition pathways. Table 2 records their decomposition temperatures, and the TGA curves are shown in Figure S3.
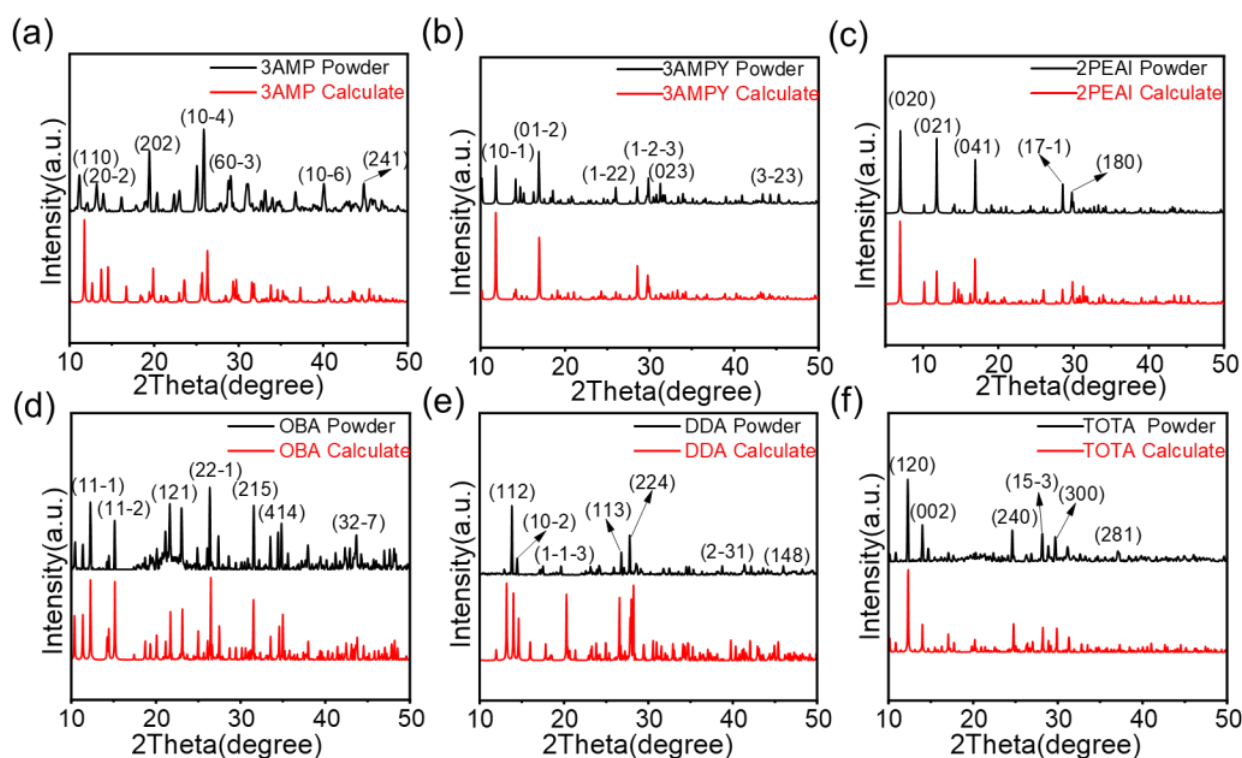
**Figure 6.** (**a**–**f**) Powder XRD patterns of hybrid gold-based perovskite derivatives with the calculated XRD patterns of the single crystals.

**Table 2.** The decomposition temperatures of hybrid gold-based perovskite derivatives.

| Compound | 3AMP | 3AMPY | 2PEAI | OBA | DDA | TOTA |
|---|---|---|---|---|---|---|
| Temperature (°C) | 82 | 98 | 104 | 102 | 94 | 110 |

The thermal decomposition processes of the six compounds can be described using two modes:

(1) For 3AMP, 2PEAI, 3AMPY, DDA, and TOTA, the thermal decomposition process can be divided into two steps:

  a. The first decomposition occurs around 100 °C, resulting in a weight loss of approximately 35%, corresponding to the organic cations.

  b. The second stage of decomposition begins at around 230 °C, corresponding to the loss of $I_2$. The final products are AuI and Au.

(2) For OBA, the thermal decomposition process can be divided into three steps:

  a. At around 100 °C, approximately 20% of the weight is lost, corresponding to the weight percentage of organic cations.

  b. At around 180 °C, the second stage of decomposition begins, with the loss of mass corresponding to $I_2$. At this point, the products are $AuI_3$ and Au.

  c. Around 240 °C, the final decomposition reaction occurs, with $AuI_3$ decomposing into Au and AuI. After this, the thermogravimetric curve stabilizes, indicating that the final decomposition products are AuI and Au.

Overall, due to the poor thermal stability of organic ions, all hybrid gold-based perovskite derivatives begin to decompose at around 100 °C. Their thermal stability is comparable to that of the widely used $CH_3NH_3PbI_3$ [25]. Considering that the operating temperatures of most optoelectronic devices are below 50 °C, it is evident that the thermal stability of these compounds is sufficient to support the device applications.

To investigate the optical properties of these compounds, we confirmed their light absorption ranges through ultraviolet-visible spectroscopy, as shown in Figure 7a. It can be observed that all compounds exhibited broad light absorption ranges, consistent with their black crystal morphology characteristics, indicating their excellent light absorption performance. Among these compounds, 3AMPY, 3AMP, OBA, and TOTA exhibited the broadest absorption peaks, reaching 1160 nm, 1150 nm, 1150 nm, and 1130 nm, respectively, while the absorption peaks of 2PEAI and DDA were relatively narrower, at 1090 nm and 1000 nm, respectively. According to the formula $Eg = 1240/\lambda_g$ (where $\lambda_g$ is the absorption threshold), the wider the absorption wavelength range, the smaller the bandgap. Therefore, all six abovementioned compounds exhibited relatively narrow bandgaps, around 1.10 eV. These materials featured broad absorption peaks ranging from visible light to near-infrared, demonstrating their potential applications in photodetection.
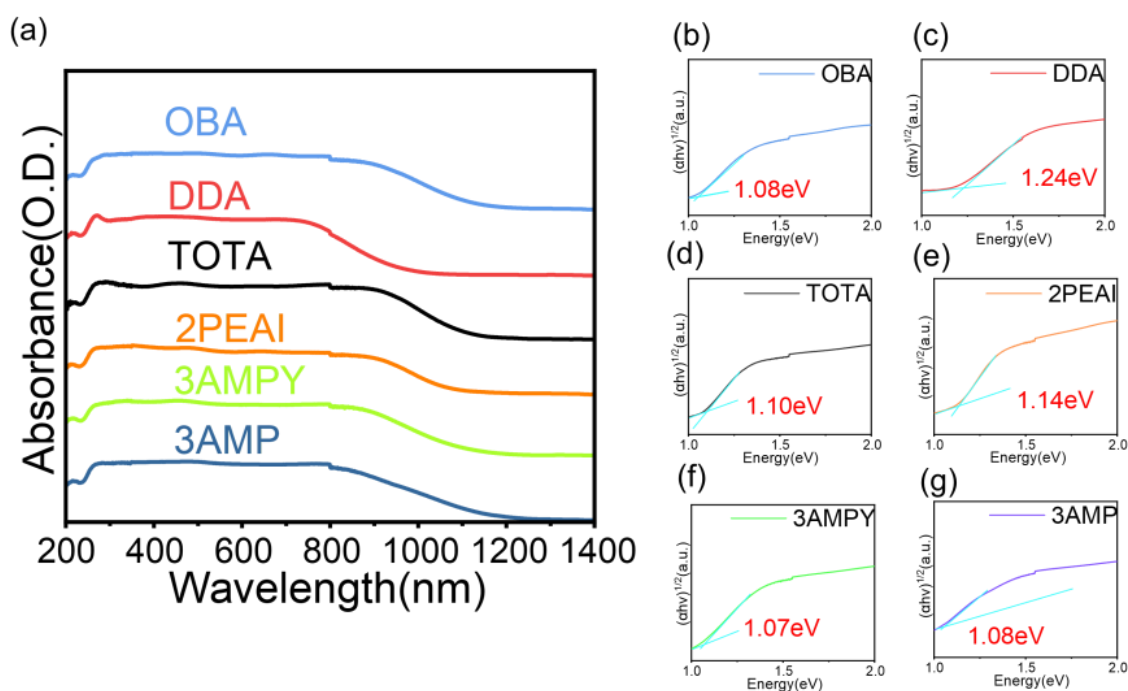


**Figure 7.** (**a**) Ultraviolet-visible absorption spectra of hybrid gold-based perovskite derivatives and (**b**–**g**) the bandgap values calculated with the Tauc plot formula.

According to the results obtained from PBE calculations (Figure 8), all the materials were indirect bandgap semiconductors. Then, we calculated the precise bandgaps of these gold-based perovskite derivatives using the Tauc plot formula for indirect bandgaps. The specific bandgap plot is shown in Figure 7b–g, where the bandgap values for OBA, DDA, TOTA, 2PEAI,3AMPY, and 3AMP are 1.08 eV, 1.24 eV, 1.10 eV, 1.14 eV, 1.07 eV, and 1.08 eV, respectively. The bandgap values of the hybrid gold-based perovskite derivatives were comparable to those reported in the literature, such as those for $[NH_3(CH_2)_7NH_3]_2$ $[(AuI_2)(AuI_4)(I_3)_2]$ (1.12 eV) and $[NH_3(CH_2)_8NH_3]_2[(AuI_2)(AuI_4)(I_3)_2]$ (1.18 eV) [18]. The smaller bandgaps are consistent with the characteristics of similar gold-based perovskite derivatives, further demonstrating the enormous potential of these compounds in narrow-bandgap optoelectronic device applications [19].
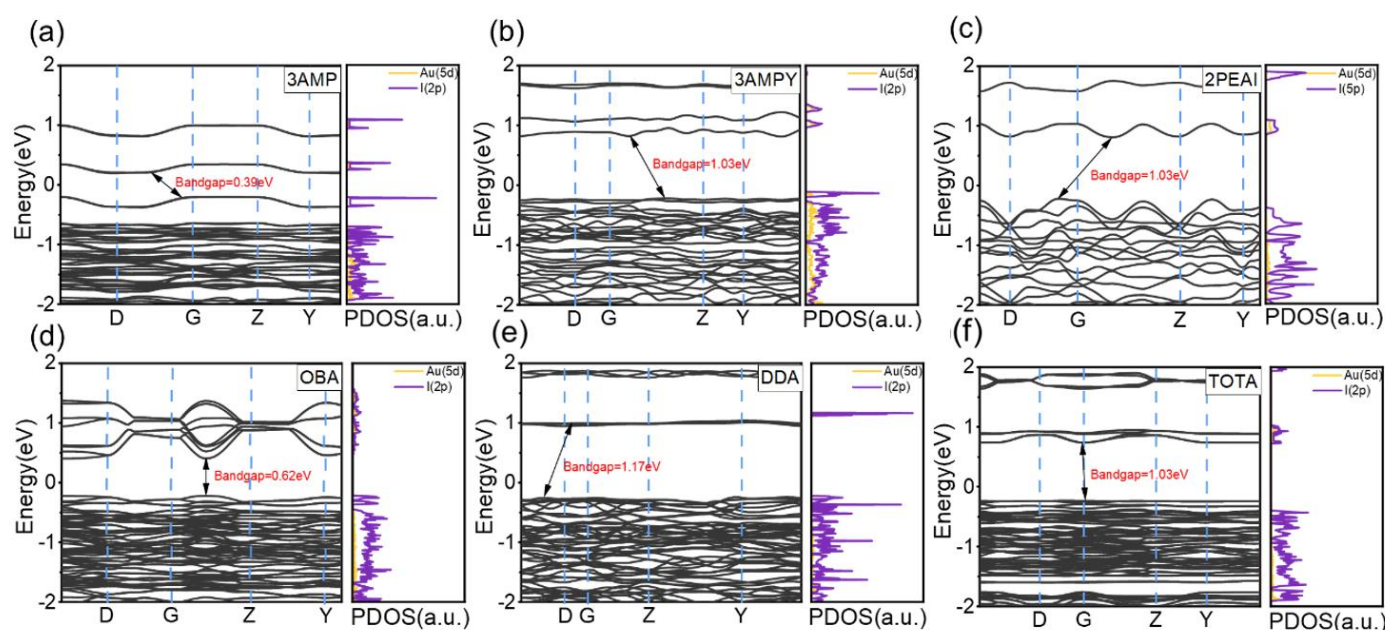
**Figure 8.** (**a**–**f**) The band structures and PDOS plots of hybrid gold-based perovskite derivatives.

### 2.4. First-Principles Calculations

For elucidating the electronic structures and semiconductor properties of hybrid gold-based perovskite derivatives, we employed the Vienna Ab initio Simulation Package (VASP) with the Perdew–Burke–Ernzerhof (PBE) function to compute the band structures and density of the states (DOS) [26,27]. As shown in Figure 8, the bandgap values obtained from the theoretical calculations for 3AMP, 3AMPY, 2PEAI, OBA, DDA, and TOTA were 1.04 eV, 1.03 eV, 1.03 eV, 0.92 eV, 1.17 eV, and 1.03 eV, respectively. These values were very close to the experimental values, demonstrating the accuracy of our computational results. For 3AMP, 3AMPY, 2PEAI, and DDA, the valence band maximum and conduction band minimum were not located in the same Brillouin zone, displaying typical characteristics of indirect bandgap semiconductors. Notably, OBA and TOTA exhibited valence-band-maximum and conduction-band-minimum positions in Brillouin zones that were very close, indicating slight indirect bandgap properties. Through analysis, it was observed that the valence band maximum and conduction band minimum of all six materials were primarily composed of I-2p orbitals (shown in purple) and a small amount of Au-5d orbitals (shown in yellow). This indicates that the narrow bandgap characteristics of these materials originate from contributions of I-2p orbitals and partial Au-5d orbitals, which is consistent with previous reports. This suggests that the strong intermolecular interactions between the structural units composed of gold and iodine ions lead to the narrow bandgap of gold-based perovskite derivatives [21].

Then, the PBE method was utilized to calculate the optical absorption coefficients of these hybrid gold-based perovskite derivatives and evaluate their potential as absorber layers in solar cells. As shown in Figure 9a,b, all compounds exhibited excellent light absorption performance, with absorption coefficients in the visible region reaching the order of $10^5$ cm$^{-1}$. Subsequently, SLME (Shockley–Queisser Limit Maximum Efficiency) calculations were performed to explore their potential as absorber layers in solar cells. The results, as shown in Figure 9c,d, indicated that when the film thickness was 500 nm, the SLME of DDA, 2PEAI, 3AMPY, and TOTA reached 32.06%, 31.89%, 30.56%, and 30.00%, respectively. These values exceeded the theoretical maximum efficiency of mainstream hybrid perovskite materials [28], demonstrating the tremendous potential of these compounds in photovoltaic applications. The great SLME values were mainly attributed to their appropriate bandgaps (around 1.10 eV) and high optical absorption coefficients. However, OBA and 3AMP exhibited relatively lower SLME values, at 18.52% and 15.26%, respec-

tively. This was due to their lower optical absorption coefficients. Recently, experimental values for methylammonium-formamidinium-based perovskite cells exceeded 20%, with the highest recorded value reaching 26.00%, approaching its theoretical maximum limit efficiency [29,30]. Although SLME does not consider factors such as carrier mobility and intrinsic defects in actual thin films, our work still reveals the application potential of these hybrid gold-based perovskite derivatives, laying the foundation for future research on their practical applications.
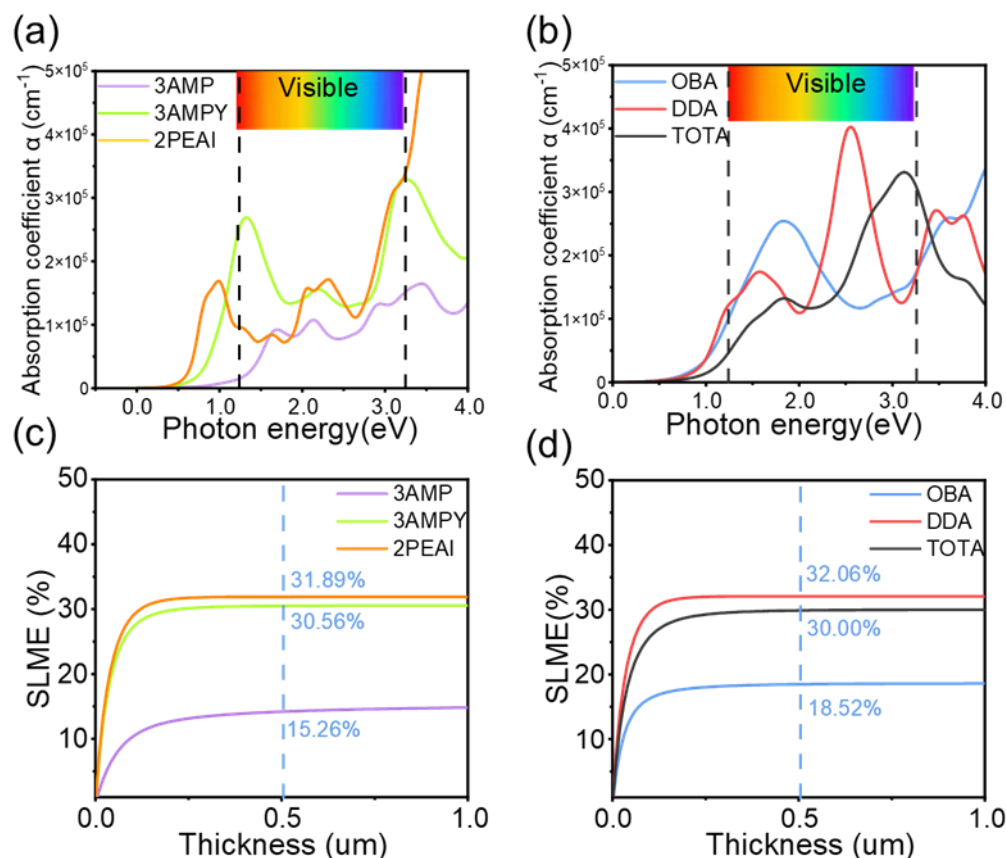


**Figure 9.** The optical properties of hybrid gold-based perovskite derivatives. (**a**,**b**) Calculated absorption spectra of average optical directions. (**c**,**d**) SLME as a function of film thicknesses.

### 3. Materials and Methods

*3.1. Materials*

All initial precursor materials and solvents were procured from commercial sources and employed without subsequent purification processes: gold (III) chloride hydrate (98.0%), 3-(Aminomethyl)piperidine (99.0%), 3-(Aminomethyl)pyridine (98.0%), 2-Phenylethylamine (99.0%), 2-2′Oxybis(ethylamine) dihydrochloride (98.0%), 1,8-Diamino-3,6-dioxaoctane (98.0%), and 4,7,10-Trioxa-1,13-tridecanediamine (98.0%), were purchased from Innochem. The hydroiodic acid (57 wt% in $H_2O$) solution was purchased from Aladdin.

*3.2. Synthesis of Single Crystals*

Millimeter-scale single crystals of gold-based perovskite derivatives can be obtained by the hydrothermal method under the appropriate parameters, the detailed steps of which are discussed in Section 2.

*3.3. Characterizations*

X-ray diffraction (XRD). XRD patterns of the films were obtained from an X-ray diffractometer (Miniflex 600, Rigaku, Japan) with Cu Kα radiation. Analysis of Single Crystal Structures. The SCs' structures were determined using a Bruker SMART APEX-II diffrac-

tometer equipped with a CCD detector (graphite-monochromatized Mo-Kα radiation, λ = 0.70 Å) at 200K. Data integration and cell refinement were performed using APEX3 software 1.5. The structure was analyzed by direct methods and refined using the SHELXTL 97 software 2.0 package. All nonhydrogen atoms of the structure were refined with anisotropic thermal parameters, and the refinements converged for $Fo^2 > 2\sigma IJFo^2$. All the calculations were performed using the SHELXTL crystallographic software 2.0 package. Symmetry analysis on the model using PLATON revealed that no noticeable space group change was needed. In the refinement, the commands EDAP and EXYZ were used to restrain some of the related bond lengths and bond angles. Raman spectroscopy. Raman spectroscopy measurements were performed on a laser Raman microscopy system (RAMAN 11, Nanophoton, Japan) at 300 K. The excitation laser wavelength was 532 nm, the energy was 2.67mW, and the detection range was 100 μm × 100 μm (the delay was 2 μm). UV−vis−NIR Absorption and Reflection Spectra Measurements. The UV−vis−NIR absorption and reflection spectra of powders were measured using a spectrophotometer (Cary 5000, Agilent, Malaysia) over the spectral range of 200–1400 nm. Thermogravimetric Analysis (TGA) Measurements. Thermogravimetric analysis (TGA) was conducted employing a TGA/DSC1/1600HT apparatus (Mettler Toledo, Switzerland). The specimens were positioned within platinum crucibles and subjected to incremental heating from an ambient temperature to 600 °C at a rate of 5 °C min$^{-1}$ under a continuous nitrogen flow. Computational Methods. The first-principles density functional theory (DFT) simulations were performed with the Vienna ab initio simulation package (VASP) to study the geometric and electronic structures of the Au-based perovskites series. We adopted the Perdew–Burke–Ernzerhof (PBE) function in the generalized gradient approximation (GGA) to optimize their geometrical structure. For geometric optimization, the Monkhorst–Pack k-point grid was configured as 2*9*3, while for self-consistent calculations, it was adjusted to 4*6*7. Our investigations adopted the PBE function to calculate the band structures. Projector augmented wave pseudopotentials with a cut-off energy of 520 eV were employed.

## 4. Conclusions

In response to the limited research on the synthesis and application potential of gold-based perovskite derivatives, we efficiently synthesized single crystals of six such derivatives through parameter optimization. Through chemical reaction studies and crystal structure analyses, we elucidated the formation of various structural units in these derivatives, deepening our understanding of their compositions. Thermogravimetric testing demonstrated their good thermal stability, with decomposition temperatures around 100 °C, akin to that of CH3NH3PbI3. Integration of experimental characterization with theoretical calculations revealed optical bandgaps of 1.10 eV and high absorption coefficients across all materials. Notably, SLME calculations indicated that DDA, 2PEAI, 3AMPY, and TOTA achieved SLME values of around 30%, underscoring their potential in photovoltaic applications. This study establishes a robust framework for employing hybrid gold-based perovskite derivatives in photodetectors and photovoltaics.

**Supplementary Materials:** The following supporting information can be downloaded at: https://www.mdpi.com/article/10.3390/inorganics12060157/s1, Figure S1. The elemental gold produced by the decomposition of products at high temperatures under an optical microscope (100×); Figure S2. (a,b) The length of the Au-I bonds in the 3AMP and 3AMPY structures; Figure S3. (a–f) The thermogravimetric analysis (TGA) curves of gold-based perovskite derivatives; Table S1. Crystal structure information of 2PEAI, 3AMP, and 3AMPY; Table S2. Crystal structure information of OBA, DDA, and TOTA.

**Author Contributions:** C.L. and P.G. conceived and designed the project. C.L., Z.Z. and Z.-A.N. prepared and characterized the properties. X.F. and L.M. assisted in the first-principles calculation. All authors discussed the results and contributed to the writing of this paper. All authors have read and agreed to the published version of the manuscript.

## References

1. Gao, P.; Grätzel, M.; Nazeeruddin, M.K. Organohalide Lead Perovskites for Photovoltaic Applications. *Energy Environ. Sci.* **2014**, *7*, 2448–2463. [CrossRef]
2. Gao, P.; Bin Mohd Yusoff, A.R.; Nazeeruddin, M.K. Dimensionality Engineering of Hybrid Halide Perovskite Light Absorbers. *Nat. Commun.* **2018**, *9*, 5028. [CrossRef]
3. Jena, A.K.; Kulkarni, A.; Miyasaka, T. Halide Perovskite Photovoltaics: Background, Status, and Future Prospects. *Chem. Rev.* **2019**, *119*, 3036–3103. [CrossRef]
4. Park, J.; Kim, J.; Yun, H.-S.; Paik, M.J.; Noh, E.; Mun, H.J.; Kim, M.G.; Shin, T.J.; Seok, S.I. Controlled Growth of Perovskite Layers with Volatile Alkylammonium Chlorides. *Nature* **2023**, *616*, 724–730. [CrossRef]
5. Dou, L.; Yang, Y.; You, J.; Hong, Z.; Chang, W.-H.; Li, G.; Yang, Y. Solution-Processed Hybrid Perovskite Photodetectors with High Detectivity. *Nat. Commun.* **2014**, *5*, 5404. [CrossRef]
6. Li, N.; Jia, Y.; Guo, Y.; Zhao, N. Ion Migration in Perovskite Light-Emitting Diodes: Mechanism, Characterizations, and Material and Device Engineering. *Adv. Mater.* **2022**, *34*, 2108102. [CrossRef]
7. Babayigit, A. Toxicity of Organometal Halide Perovskite Solar Cells. *Nat. Mater.* **2016**, *15*, 247–251. [CrossRef]
8. Lyu, M.; Yun, J.; Chen, P.; Hao, M.; Wang, L. Addressing Toxicity of Lead: Progress and Applications of Low-Toxic Metal Halide Perovskites and Their Derivatives. *Adv. Energy Mater.* **2017**, *7*, 1602512. [CrossRef]
9. Xiao, Z.; Song, Z.; Yan, Y. From Lead Halide Perovskites to Lead-Free Metal Halide Perovskites and Perovskite Derivatives. *Adv. Mater.* **2019**, *31*, e1803792. [CrossRef]
10. Igbari, F.; Wang, Z.-K.; Liao, L.-S. Progress of Lead-Free Halide Double Perovskites. *Adv. Energy Mater.* **2019**, *9*, 1803150. [CrossRef]
11. Ghosh, B.; Febriansyah, B.; Harikesh, P.C.; Koh, T.M.; Hadke, S.; Wong, L.H.; England, J.; Mhaisalkar, S.G.; Mathews, N. Direct Band Gap Mixed-Valence Organic–Inorganic Gold Perovskite as Visible Light Absorbers. *Chem. Mater.* **2020**, *32*, 6318–6325. [CrossRef]
12. Gupta, S.D. The double auric iodides of substituted ammonium bases. *J. Am. Chem. Soc.* **1914**, *36*, 747–751. [CrossRef]
13. Strähle, J.; Gelinek, J.; Kölmel, M. Über den thermischen Abbau einiger Alkalimetall- und Ammoniumhalogenoaurate(III) und die Kristallstruktur der Zersetzungsprodukte $Rb_2Au_2Br_6$, $Rb_3Au_3Cl_8$ und $Au(NH_3)Cl_3$. *Z. Anorg. Allg. Chem.* **1979**, *456*, 241–260. [CrossRef]
14. Strähle, J.; Bärnighausen, H. Notizen: Die Kristallstruktur von Rubidium-tetrachloro-aurat(III) $RbAuCl_4$. *Z. Naturforschung B* **1970**, *25*, 1186–1187. [CrossRef]
15. Kojima, N.; Kitagawa, H.; Ban, T.; Amita, F.; Nakahara, M. Semiconductor-to-Metal and Metal-to-Metal Transitions in the Three-Dimensional Mixed-Valence Compound $Cs_2Au_2I_6$ under High Pressures. *Solid State Commun.* **1990**, *73*, 743–745. [CrossRef]
16. Debbichi, L.; Lee, S.; Cho, H.; Rappe, A.M.; Hong, K.; Jang, M.S.; Kim, H. Mixed Valence Perovskite $Cs_2Au_2I_6$: A Potential Material for Thin-Film Pb-Free Photovoltaic Cells with Ultrahigh Efficiency. *Adv. Mater.* **2018**, *30*, 1707001. [CrossRef]
17. Li, W.; Li, Y.; Zhang, Z.; Gao, P. Alternative Lead-Free Mixed-Valence Double Perovskites for High-Efficiency Photovoltaic Applications. *J. Energy Chem.* **2023**, *84*, 347–353. [CrossRef]
18. Fan, Y.; Liu, Q.; Zhang, Z.; Lien, S.-Y.; Xie, Y.; Liang, W.; Gao, P. Gold-Based Double Perovskite-Related Polymorphs: Low Dimensional with an Ultranarrow Bandgap. *Chem. Mater.* **2022**, *34*, 1544–1553. [CrossRef]
19. Walusiak, B.W.; Raghavan, A.; Cahill, C.L. $I^-/I3^-$ Redox-Assisted Synthesis and Properties of Low Dimensional, Mixed-Valent Gold Iodide Perovskite Derivatives. *Cryst. Growth Des.* **2024**, *24*, 678–687. [CrossRef]
20. Evans, H.A.; Schueller, E.C.; Smock, S.R.; Wu, G.; Seshadri, R.; Wudl, F. Perovskite-Related Hybrid Noble Metal Iodides: Formamidinium Platinum Iodide $[(FA)_2Pt^{IV}I_6]$ and Mixed-Valence Methylammonium Gold Iodide $[(MA)_2Au^IAu^{III}I_6]$. *Inorg. Chim. Acta* **2017**, *468*, 280–284. [CrossRef]
21. Starkholm, A.; Kloo, L.; Svensson, P.H. Gold Polyiodide Hybrid Perovskite Solar Cells. *ACS Mater. Lett.* **2023**, *5*, 406–412. [CrossRef]
22. Braathen, G.; Chou, P.-T.; Frei, H. Time-resolved reaction of oxygen (1.DELTA.) with iodide in aqueous solution. *J. Phys. Chem.* **1988**, *92*, 6610–6615.
23. Murasugi, H.; Kumagai, S.; Iguchi, H.; Yamashita, M.; Takaishi, S. Organic–Inorganic Hybrid Gold Halide Perovskites: Structural Diversity through Cation Size. *Chem. A Eur. J.* **2019**, *25*, 9885–9891. [CrossRef]
24. Kojima, Norimichi, Gold Valence Transition and Phase Diagram in the Mixed-Valence Complexes, $M2[Au^IX_2][Au^{III}X_4]$ (M = Rb, Cs; X = Cl, Br, and I). *Bull. Chem. Soc. Jpn.* **2000**, *73*, 1445–1460. [CrossRef]
25. Wu, Y.; Xie, F.; Chen, H.; Yang, X.; Su, H.; Cai, M.; Zhou, Z.; Noda, T.; Han, L. Thermally Stable $MAPbI_3$ Perovskite Solar Cells with Efficiency of 19.19% and Area over 1 cm $^2$ Achieved by Additive Engineering. *Adv. Mater.* **2017**, *29*, 1701073. [CrossRef]

26. Kresse, G.; Furthmüller, J. Efficiency of Ab-Initio Total Energy Calculations for Metals and Semiconductors Using a Plane-Wave Basis Set. *Comput. Mater. Sci.* **1996**, *6*, 15–50. [CrossRef]
27. Kresse, G.; Joubert, D. From Ultrasoft Pseudopotentials to the Projector Augmented-Wave Method. *Phys. Rev. B* **1999**, *59*, 1758–1775. [CrossRef]
28. Monika; Pachori, S.; Agrawal, R.; Choudhary, B.L.; Verma, A.S. An Efficient and Stable Lead-Free Organic–Inorganic Tin Iodide Perovskite for Photovoltaic Device: Progress and Challenges. *Energy Rep.* **2022**, *8*, 5753–5763. [CrossRef]
29. Machín, A.; Márquez, F. Advancements in Photovoltaic Cell Materials: Silicon, Organic, and Perovskite Solar Cells. *Materials* **2024**, *17*, 1165. [CrossRef]
30. Lu, X.; Fan, X.; Zhang, H.; Xu, Q.; Ijaz, M. Review on Preparation of Perovskite Solar Cells by Pulsed Laser Deposition. *Inorganics* **2024**, *12*, 128. [CrossRef]